



Surface plasticity in laser scanning of metals

Yazhuo Liu ^a , Kunqing Ding ^a, Andrew J. Birnbaum ^b, Anna Rawlings ^b, Audrey Sun ^a , Wen Chen ^c, David L. McDowell ^a , John G. Michopoulos ^b , Ting Zhu ^{a,*}

^a George W. Woodruff School of Mechanical Engineering, Georgia Institute of Technology, Atlanta, GA 30332, USA

^b US Naval Research Laboratory, WA, DC 20375, USA

^c Department of Aerospace and Mechanical Engineering, University of Southern California, Los Angeles, CA 90089, USA

ARTICLE INFO

Keywords:

Additive manufacturing
Laser processing
Crystal plasticity
Metals
Finite element modeling

ABSTRACT

Laser-based additive manufacturing causes residual stresses and surface distortion of as-built components, significantly affecting their fracture and fatigue resistance in service. Despite extensive studies, the influence of thermomechanical history on near-surface plastic deformation in laser-scanned metal crystals remains unclear. Using optical microscopy, we visualize residual surface plastic deformation along single laser tracks on nickel single crystals, revealing slip trace distributions that depend on laser power and scan direction. Crystal plasticity finite element (CPFE) simulations capture the evolution of stress and plastic strain fields along laser tracks, predicting slip trace patterns in agreement with experimental observations. Furthermore, experimentally observed slip traces are correlated with CPFE-simulated subsurface stress evolution, underscoring the role of thermomechanical history in laser scan-induced surface plasticity. Our integrated experimental and modeling study advances predictive modeling of printing-induced residual stresses and distortion in additively manufactured components.

1. Introduction

Additive manufacturing (AM), also known as 3D printing, is transforming various industries by enabling design and production possibilities previously unattainable [1]. Laser powder bed fusion (LPBF) and laser direct energy deposition (LDED) are widely used AM methods for metal 3D printing due to its ability to fabricate virtually any shape, achieve relatively high resolution, and accommodate diverse material options [2]. Laser-based processing typically involves rapid cooling, steep temperature gradients, and repeated thermal cycling [3]. These extreme conditions produce complex microstructures and induce heterogeneous thermo-elastic-plastic deformation, leading to significant stresses, defect formation, and degradation in service [4,5]. Notably, laser scanning induces residual stresses and surface distortion in as-built components, significantly impacting their fracture and fatigue resistance in service. Therefore, understanding the generation and evolution of printing-induced near-surface stresses and plastic strains is crucial for producing high-performance AM components.

Extensive experimental and modeling efforts have been dedicated to investigating AM processes, including heat and mass transfer, fluid flow, and the formation of solidification microstructures and defects [6–10].

However, due to insufficient experimental input and validation at adequate spatial and temporal resolution, reliable prediction of printing-induced stresses and plastic strains in AM parts remains challenging. Experimental studies have characterized stresses in AM parts using techniques such as lab-scale X-ray diffraction [11], synchrotron diffraction [12], neutron diffraction [13], digital image correlation [14], and electron backscatter diffraction [15]. Additionally, numerical simulations based on phenomenological J_2 plasticity [16,17] and crystal plasticity [18,19] models have been conducted to analyze how AM processing influences residual stresses and distortion in AM parts. However, coupled experimental and modeling research regarding crystal plasticity effects in the evolution of printing-induced stresses and plastic strains remains limited, restricting the ability to develop predictive models for these phenomena in AM parts.

Fundamental study of crystal plasticity during laser-processing of materials is critical for understanding the effects of thermomechanical history, plastic anisotropy, and irreversibility during AM processing. Recently, Birnbaum et al. [20] developed an optical method to visualize near-surface plastic deformation that occurs along a single laser track. Using nickel (Ni) single crystals, they observed slip traces generated on the crystal surface during laser scanning, revealing the mode and extent

* Corresponding author.

E-mail address: ting.zhu@me.gatech.edu (T. Zhu).

of plastic shearing and the associated dislocation movement on active slip systems. In this work, we integrate such slip trace experiments with crystal plasticity finite element (CPFE) simulations to gain deeper insights into surface plasticity in laser scanning of Ni single crystals. The use of pure single crystals reduces complexities arising from grain and dendrite growth during laser scanning [21,22], providing a solid foundation for future investigations of polycrystalline metals and alloys. Our temperature-dependent CPFE model incorporates the effects of thermal softening, melting, cooling, and solidification on plastic shear. We compare the CPFE predictions and experimental observations of slip trace patterns, in order to establish mechanistic links between thermo-mechanical history and near-surface elastic-plastic deformation along individual laser tracks. This integrated experimental and modeling approach advances predictive modeling of printing-induced stresses and distortion in AM components.

2. Experimental

We created single laser tracks on the surface of ultra-high purity Ni single crystals using the method of Birnbaum et al. [20]. Prior to scanning, Ni baseplates were ground and polished (down to 40 nm colloidal silica) to ensure an initially featureless surface. Single tracks were generated using an M2 Concept LPBF system with laser powers of 50–400 W, scanning speeds of 100–550 mm/s, and a Gaussian laser spot

size of 120 μm (wavelength 1064 nm). Surface slip traces were visualized using a Keyence UHX-6000 digital optical microscope.

Fig. 1(a) and **(b)** show top-view micrographs of the (111) surface of a face-centered cubic (FCC) Ni single crystal with a 220 W, 550 mm/s laser track along the $[\bar{1}2\bar{1}]$ and $[\bar{1}01]$ scan directions, respectively. The laser-scanned region maintains the single-crystal nature of the base metal without forming grains and dendrites. Each track terminates within the sample surface, leaving a straight fusion zone (FZ) between two parallel boundaries. The FZ width is about 120 μm , similar to the laser spot size. For the $[\bar{1}2\bar{1}]$ scan direction, slip traces are symmetric about the track centerline, with three types marked by different colored lines, and the angle between the inclined slip traces and the laser track is $\sim 30^\circ$. In contrast, for the $[\bar{1}01]$ scan direction, slip traces are asymmetric, showing three distinct types, with the corresponding angle $\sim 60^\circ$. The symmetric slip traces in **Fig. 1(a)** resemble the waves and wake lines generated by a fast-moving boat in still water [23]. However, unlike transient waves that fade and eventually disappear, these slip traces are permanent. Furthermore, the asymmetric slip traces in **Fig. 1(b)** highlight the strong influence of anisotropic plastic flow in crystals, in contrast to the isotropic flow in fluids.

In FCC Ni, the observed slip traces result from surface steps generated by surface-exiting dislocations on {111} slip planes with Burgers vectors along $\langle 110 \rangle$ slip directions. **Fig. 1(c)** presents a three-dimensional view of the Thompson tetrahedron, illustrates three

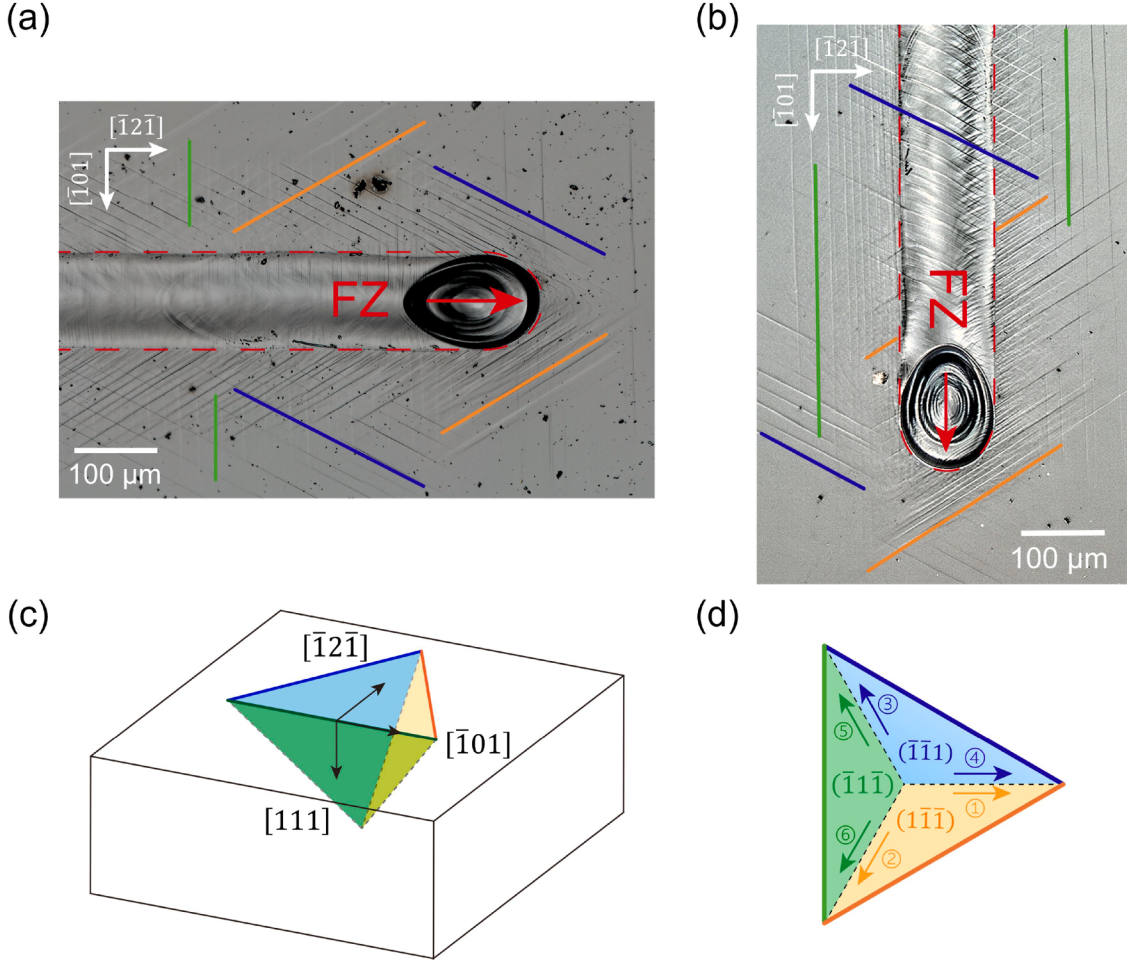


Fig. 1. Experimental observations of plastic deformation along single laser tracks of Ni single crystals. The laser power is 220 W, scanning speed is 550 mm/s and spot size is 120 μm . Top-view micrographs of the (111) surface are shown for laser scanning along **(a)** $[\bar{1}2\bar{1}]$ and **(b)** $[\bar{1}01]$ directions. The red dashed line marks the boundary of the fusion zone (FZ). The blue, green and orange solid lines represent slip traces created by the intersection of the $(\bar{1}\bar{1}1)$, $(\bar{1}\bar{1}\bar{1})$ and $(1\bar{1}\bar{1})$ planes with the (111) surface, respectively. **(c)** A 3D schematic of the Thompson tetrahedron aligned with the orientation of the tested Ni single crystal, showing three inclined {111} slip planes (distinguished by different colors) intersecting the top (111) surface. **(d)** The Thompson tetrahedron viewed along the [111] surface normal.

inclined $\{111\}$ planes (shown in different colors) intersecting the top (111) surface. The angles of the inclined slip traces relative to the laser track in Fig. 1(a,b) are consistent with the geometrical relationships illustrated in Fig. 1(c). Dislocations on these slip planes generate the three observed types of slip traces, which align with the $\langle 110 \rangle$ directions on the (111) surface, as marked by the blue, green, and orange solid lines. Since dislocations with slip planes or slip directions parallel to the (111) surface do not create surface steps, only six of the twelve $\{111\}\langle 110 \rangle$ slip systems contribute directly to these slip traces, which are numbered in Fig. 1(d). Furthermore, each inclined $\{111\}$ slip plane contains two $\langle 110 \rangle$ slip directions that can potentially produce surface steps. However, the active $\langle 110 \rangle$ directions cannot be directly inferred from the observed slip traces; instead they can be determined through CPFE simulations.

3. Model and simulation

3.1. Crystal plasticity model

Crystal plasticity constitutive relations are formulated within the rate-dependent, finite strain framework of elastic-plastic deformation in single crystals [24]. The total deformation gradient tensor \mathbf{F} is expressed using a multiplicative decomposition [25]

$$\mathbf{F} = \mathbf{F}^e \mathbf{F}^p \mathbf{F}^0 \quad (1)$$

where \mathbf{F}^e is the elastic deformation gradient, \mathbf{F}^p is the plastic deformation gradient, and \mathbf{F}^0 is the thermal deformation gradient accounting for thermal expansion and contraction.

The elastic Green-Lagrange strain tensor is given by $\mathbf{E}^e = \frac{1}{2} (\mathbf{F}^{eT} \mathbf{F}^e - \mathbf{I})$, where \mathbf{I} is the second-order identity tensor. The second Piola-Kirchhoff stress is calculated as $\mathbf{T}^* = \mathbf{C} : \mathbf{E}^e$, where \mathbf{C} is the fourth-order elasticity tensor for a single crystal. To capture the temperature effects on \mathbf{C} , two non-dimensional factors, $\phi(T)$ and $\xi(T) \in [0, 1]$, are introduced, i.e.,

$$C = \xi(T)\phi(T)\tilde{\mathbf{C}} \quad (2)$$

where T is the absolute temperature in Kelvin and $\tilde{\mathbf{C}}$ is the elasticity tensor at room temperature T_0 . The components of $\tilde{\mathbf{C}}$ in the local crystal basis are $\tilde{C}_{ijkl} = C_{12}\delta_{ij}\delta_{kl} + C_{44}(\delta_{ik}\delta_{jl} + \delta_{il}\delta_{jk}) + (C_{11} - C_{12} - 2C_{44})d_{ijkl}$, where δ_{ij} is the Kronecker delta and the only non-zero components of d_{ijkl} are $d_{1111} = d_{2222} = d_{3333} = 1$. The temperature-dependent functions $\phi(T)$ and $\xi(T)$ are defined as

$$\phi(T) = 1 - \eta(T - T_0)/(T_m - T_0) \quad (3)$$

$$\xi(T) = 1 - \theta/(T_m - T + \theta) + \theta/(T_m - T_0 + \theta) \quad (4)$$

where T_m is the melting temperature, η is the softening coefficient, and θ is the reference temperature, taken as 10 K in our simulations. In Eq. (3), $\phi(T)$ decreases linearly with temperature, reflecting the thermal softening of the elasticity tensor. In Eq. (4), $\xi(T)$ decreases gradually at lower temperatures but drops sharply near the melting point, indicating the loss of elastic stiffness during the phase transition from solid to liquid.

Assuming isotropic thermal expansion for a cubic crystal with a temperature-independent coefficient α , we define $\mathbf{F}^0 = \sqrt{1 + 2\alpha(T - T_0)} \mathbf{I}$. The rate of the plastic deformation gradient is given by $\dot{\mathbf{F}}^p = \mathbf{L}^p \mathbf{F}^p$, where \mathbf{L}^p is the plastic velocity gradient expressed as a superposition of the plastic shearing rates on the twelve $\{111\}\langle 110 \rangle$ slip systems in an FCC crystal, i.e.,

$$\mathbf{L}^p = \sum_{i=1}^{12} \dot{\gamma}_i^p \mathbf{m}_i \otimes \mathbf{n}_i \quad (5)$$

Here, \mathbf{m}_i and \mathbf{n}_i are unit vectors representing the slip direction and the slip plane normal, respectively. The plastic shearing rate on the i th slip system depends on both stress and temperature [26], and follows the Kocks-Argon-Ashby flow rule [27]

$$\dot{\gamma}_i^p = \dot{\gamma}_0 \exp \left(- \frac{\Delta F}{k_B T} \left[1 - \left(\frac{|\tau_i|}{s_i} \right)^p \right]^q \right) \operatorname{sign}(\tau_i) \quad (6)$$

where k_B is the Boltzmann constant, $\dot{\gamma}_0$ is the reference shearing rate, τ_i is the resolved shear stress, ΔF is the activation energy for dislocation motion at $\tau_i = 0$, p and q are nonlinear profiling parameters. In Eq. (6), s_i is the resistance to dislocation motion. It has an initial value s_0 , identical for all 12 slip systems, and evolves according to $\dot{s}_i = \sum_j h_{ij} |\dot{\gamma}_j^p|$ where $h_{ij} = q_{ij} h_0 (1 - s_j/s_{\text{sat}})^{a_h}$, with $q_{ij} = q_1 + (1 - q_1)\delta_{ij}$ and the hardening parameters h_0 , a_h , and s_{sat} identical for all slip systems.

Additionally, when the temperature T in a material element reaches the melting point T_m , the plastic strains are reset to zero [19], and the slip resistance reverts to its initial value s_0 . As the material subsequently cools below T_m , plastic strain accumulation restarts. This treatment is used to approximate the effects of cooling-induced plastic flow for cases with and without melting, corresponding to laser scans with high and low power, as discussed later.

3.2. Simulation setup

To investigate thermo-elastic-plastic deformation during laser scanning, we performed crystal plasticity finite element (CPFE) simulations of a laser beam travelling on the surface of Ni single crystals. The CP model described in Section 3.1 was implemented in ABAQUS/Explicit by writing a user material subroutine (VUMAT) with material parameters listed in Table 1. The FE model is a rectangular box with dimensions of 3 mm \times 1.5 mm \times 1.5 mm. The mesh consists of 240,000 C3D8R elements with a higher density near the laser track. The moving Cartesian coordinate system is placed at the center of the melt pool, with its axes defined as x -[12̄1], y -[101], and z -[111], as illustrated in Fig. 2(a). All sides of the simulation box are traction-free, except for the bottom surface where normal displacements are zero.

The traveling laser beam generates a moving temperature field near the crystal surface [28–30]. Since this work focuses on crystal plastic deformation along laser tracks, we adopt a simplified moving temperature profile to represent the steady-state temperature distribution that keeps pace with a traveling laser beam, i.e.,

$$T(x,y,z) = T_m \exp \left\{ -\kappa \left[\frac{1}{4lw^2} \left(\log \frac{z}{ac} + \sqrt{\log^2 \frac{z}{a} + 4ly^2} \right)^2 - \frac{\log^2 c}{4lw^2} + \frac{x^2}{u^2} - 1 \right] \right\} \quad (7)$$

Here, parameter κ controls the heating and cooling rate, a sets the depth of the temperature field, w determines the melt pool size, l and c are profiling constants, and u equals w for material points ahead of the laser

Table 1
Parameters used in CPFE simulations.

C_{11} (GPa)	C_{12} (GPa)	C_{44} (GPa)	η	T_0 (K)	T_m (K)	α (K^{-1})
246.5	147.3	124.7	0.5	300	1726	13.3×10^{-6}
$\dot{\gamma}_0$ (s^{-1})	ΔF (eV)	s_0 (MPa)	s_{sat} (MPa)	p	q	h_0 (MPa)
1×10^7	5.68	150	547	0.7	1.5	600
a_h	q_1	κ	a (mm)	l	w (mm)	c (mm)
0.8	1.4	0.1	0.15	1×10^8	0.06	0.01

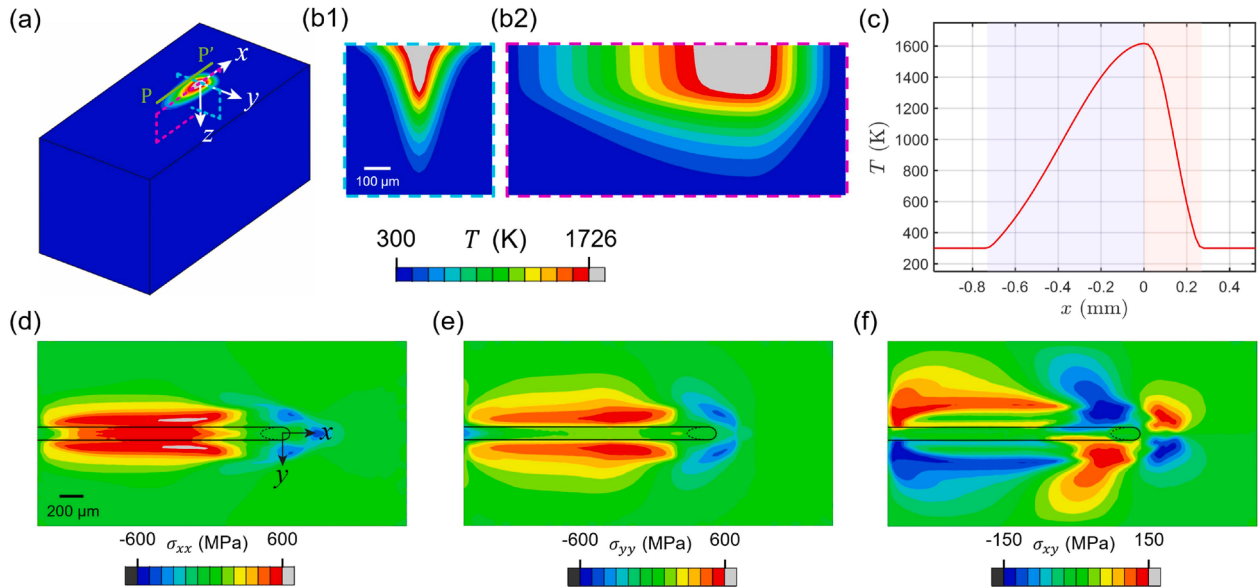


Fig. 2. CPFE results of temperature and stress distributions for laser scanning along the $x\text{-}[\overline{1}\overline{2}\overline{1}]$ direction. (a) A 3D view of the temperature profile created by a moving laser source. The moving Cartesian coordinate system was placed at the center of the melt pool with $x\text{-}[\overline{1}\overline{2}\overline{1}]$, $y\text{-}[\overline{1}01]$, and $z\text{-}[111]$. The light blue and purple dash lines indicate the cross sections shown in (b). The temperature distribution is shown in (b1) a cross section normal to the scan direction (i.e., the $y\text{-}z$ plane in (a)) and (b2) a transverse cross section along the centerline of the laser track (i.e., the $x\text{-}z$ plane in (a)). (c) Surface temperature distribution along the PP' path, with the red and blue shades indicating heating and cooling regions. (d-f) Distributions of σ_{xx} , σ_{yy} , and σ_{xy} on the top surface. The black solid line marks the FZ boundary.

beam ($x > 0$) and $3w$ otherwise ($x < 0$). These parameters provide flexible control over melt pool geometry, enabling reproduction of both the pear-shaped surface profile and the funnel-shaped cross-sectional profile. The parameter values are listed in Table 1, and the laser scan speed is set to $v_L = 0.5$ m/s. The simulated isotherms qualitatively match the melt pool shape observed in our experiments and reported in previous studies [1]. It should be noted that Eq. (7) is a simplified approximation. It neglects latent heat effects, plastic work dissipation, and the transition between conduction and keyhole modes. Consequently, while the chosen profile captures the overall melt pool geometry and provides a computationally efficient framework for analyzing crystal plasticity, the quantitative accuracy of the predicted temperature field is limited.

4. Results and discussion

4.1. $[\overline{1}\overline{2}\overline{1}]$ scan direction

For the $x\text{-}[\overline{1}\overline{2}\overline{1}]$ scan direction, Fig. 2(a) presents the simulated temperature profile on the sample surface, where the isotherms closely resemble the pear-shaped melt pool observed in Fig. 1(a). Fig. 2(b1) shows the temperature distribution in a cross section perpendicular to the scan direction (i.e., the $y\text{-}z$ plane in Fig. 2(a)), with isotherms approximating the funnel-shaped melt pool. Fig. 2(b2) displays the temperature distribution in a transverse cross section along the centerline of the laser track (i.e., the $x\text{-}z$ plane in Fig. 2(a)). In Fig. 2(c), the surface temperature along the PP' path (indicated in Fig. 2(a)) is plotted against the x -coordinate, showing the temperature variation along the surface. This temperature profile reflects the thermal history of a typical material point on the PP' path as the traveling laser beam approaches and then moves past, depicting the sequential heating and cooling experienced during the scanning process.

A non-uniform temperature distribution along a laser track induces uneven thermal expansion and contraction between neighboring material points, generating stress and elastic-plastic strain fields. Fig. 2(d-f) show CPFE-simulated in-plane normal and shear stress fields on the top (111) surface. Due to crystal symmetry, the distributions of σ_{xx} and σ_{yy} are symmetric about the track centerline, while σ_{xy} exhibits anti-

symmetry. Ahead of the melt pool, large compressive σ_{xx} and σ_{yy} (blue contours) develop as the thermal expansion of heated material near the melt pool is constrained by the surrounding cooler material. To balance these stress gradients, the anti-symmetric σ_{xy} component emerges, with a magnitude smaller than that of σ_{xx} and σ_{yy} . Behind the melt pool, large tensile σ_{xx} and σ_{yy} (red contours) arise as the contraction of cooled material is restricted by adjacent, less-cooled regions. Similarly, an anti-symmetric σ_{xy} component forms to balance stress gradients. Because of the traction-free condition on the top surface, normal and shear stress components along the z direction are zero at the surface but become nonzero below it, influencing plastic strains and slip trace formation. Based on these stress states, resolved shear stresses on individual slip systems can be calculated to estimate the slip trace distributions on the top surface using Schmid factor analysis [31]. However, this work relies on the full-field CPFE results of accumulated plastic shear strains to analyze slip trace patterns. The complex stress and strain states originate from the intricate thermal history of heating and cooling induced by the moving heat source, as further analyzed through the CPFE simulations presented below.

Fig. 3 shows CPFE-simulated distributions of the accumulated plastic shear strain, $\gamma_i^{\text{acc}} = \int_0^t |\dot{\gamma}_i^P| dt'$ on $\{111\}\langle 110 \rangle$ slip systems, which are used to identify the slip systems responsible for generating the slip traces observed in Fig. 1(a). As discussed earlier, the slip traces on the (111) surface result from surface steps created by surface-exiting dislocations on the six $\{111\}\langle 110 \rangle$ systems marked in Fig. 1(d). Fig. 3(a) presents contour plots of γ_i^{acc} for each of these six slip systems. Due to slip system symmetry (Fig. 1(d)), the γ_i^{acc} distributions on slip systems 1 and 4 are mirror images of each other about the track centerline, as are those on slip systems 2 and 3, and on slip systems 5 and 6. Based on the location and magnitude of γ_i^{acc} , we predicted the distribution of surface slip traces, as shown in Fig. 3(b). Solid orange and blue lines denote the symmetrically inclined slip traces generated by plastic shearing on slip systems 1 and 4, respectively. The γ_i^{acc} distribution along the laser track indicates that these slip traces form ahead of the melt pool due to heating-induced expansion. Their densities increase downstream as

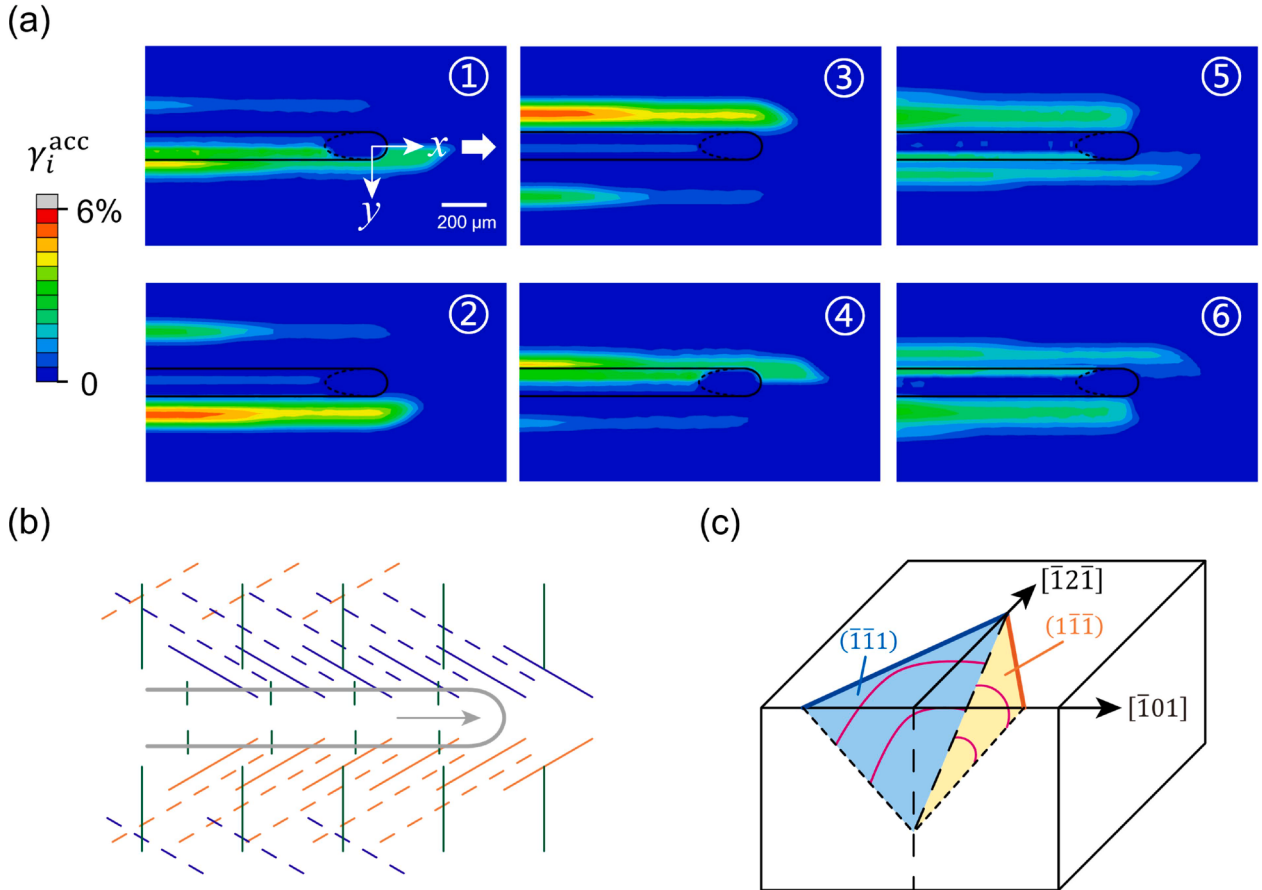


Fig. 3. CPFE results for accumulated plastic shear strains (γ_i^{acc}), slip traces and slip bands for laser scanning along the $x\text{-}[\bar{1}\bar{2}\bar{1}]$ direction. (a) Contour plots of γ_i^{acc} on the top surface for each of the six $\{111\}\langle 110 \rangle$ slip systems (marked in Fig. 1(d)) responsible for generating surface slip traces. (b) Predicted distributions of slip traces along the laser track. (c) Schematic illustration of the formation process of slip traces associated with slip systems 2 and 3: dislocations are generated at the central FZ within the crystal, glide toward the top surface, and aggregate to form slip bands. Some of these dislocations exit the top surface, creating surface steps that correspond to the slip traces marked by the dashed orange and blue lines downstream along the laser track in Fig. 3(b).

constrained contraction occurs during cooling, leading to denser slip traces near the FZ boundaries in Fig. 1(a). Moreover, dashed orange and blue lines denote the symmetrically inclined slip traces arising from plastic shearing on slip systems 2 and 3, respectively. The γ_i^{acc} distribution indicates that these slip traces predominantly form downstream due to cooling-induced contraction and correspond to the less dense traces farther from the FZ boundaries in Fig. 1(a). Additionally, solid green lines denote vertical slip traces from plastic shearing on slip systems 5 and 6. These traces exhibit significantly lower densities and form farther from the FZ boundaries, consistent with the observations in Fig. 1(a).

The above results demonstrate the consistency between CPFE predictions and experimental observations of slip traces along the laser track. Based on the location and magnitude of γ_i^{acc} , we can correlate the slip traces on the top surface with subsurface plastic deformation. Fig. 3(c) illustrates the formation process of the slip traces associated with slip systems 2 and 3: dislocations are generated at the central FZ within the crystal, glide toward the top surface, and aggregate to form slip bands. Some of these dislocations exit the top surface, creating surface steps that correspond to the slip traces marked by the dashed orange and blue lines downstream along the laser track in Fig. 3(b).

CPFE simulations were further used to predict transient and residual surface distortion and plastic strains in laser-scanned Ni single crystals. Fig. 4(a) shows a contour plot of the equivalent plastic strain ($\bar{\epsilon}_p$, reflecting the net rather than accumulated plastic strain) on the deformed top surface, while Fig. 4(b) plots the surface displacement (u_z) against the z-coordinate along P-1 to P-4 paths crossing the laser track (shaded area), as marked in Fig. 4(a). Specifically, P-1 path: ahead of the

melt pool, heating induces expansion, leading to surface bulging around the melt pool; P-2 path: across the melt pool, the surface exhibits the most significant bulging at the melt pool; P-3 and P-4 paths: behind the melt pool, cooling induces contraction, progressively reducing surface bulging downstream along the laser track. These results reveal the formation of transient and residual surface undulations driven by the non-uniform distribution of plastic strains produced during the heating-cooling cycle.

To further relate the observed surface distortion to subsurface stress and plastic strain fields, Fig. 4(c1-c2) show the distribution of σ_{xx} in the cross sections along the P-2 and P-4 paths. For the cross section along the P-2 path, significant compressive stresses develop beneath the melt pool due to constraints on heating-induced expansion. In contrast, along the P-4 path, substantial tensile stresses arise from constraints on cooling-induced contraction. Each cross section exhibits both tensile and compressive components of σ_{xx} , maintaining self-equilibrium in the absence of external mechanical loading during laser scanning. Notably, the depth-dependent distributions of σ_{xx} in Fig. 4(c1-c2) differ from the nearly thickness-independent distribution near a weld region in a thin plate (e.g., Fig. 70 in DebRoy et al. [1]), highlighting the unique near-surface stress generation phenomenon in laser-scanned bulk materials.

4.2. Effects of laser power

To investigate the effects of laser power, we modified the moving temperature field shown in Fig. 2(a-b) by scaling it down to 0.8 of its original value, ensuring that the peak temperature remained below the

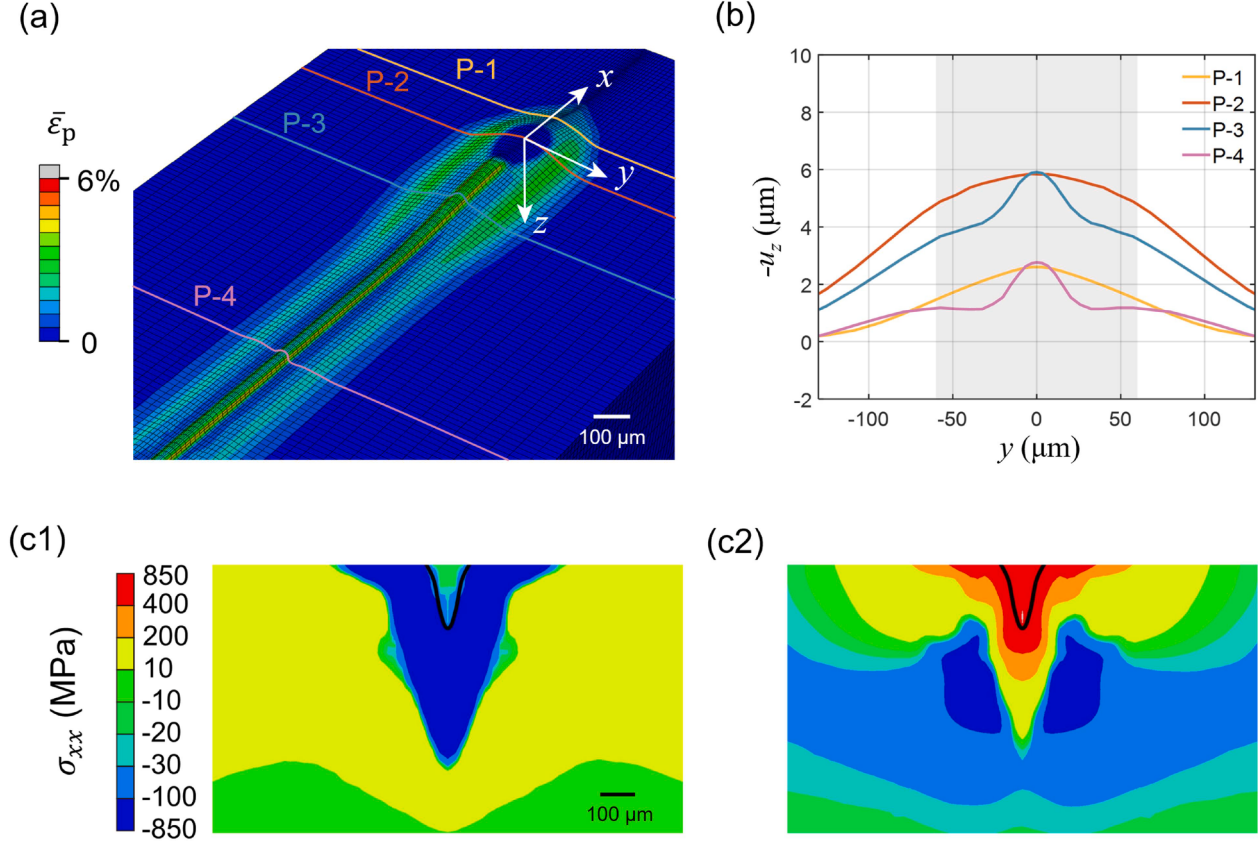


Fig. 4. CPFE results of laser scanning along the $x\text{-}[\bar{1}\bar{2}\bar{1}]$ direction. (a) Contour plots of equivalent plastic strain ($\bar{\varepsilon}_p$) on the deformed surface, with nodal displacements amplified 10 times for clear visualization. (b) Surface displacement (u_z) against the z -coordinate along four paths (P-1 to P-4 in (a)) crossing the laser track. The shaded area illustrates the extent of the fusion zone. (c1-c2) Distributions of σ_{xx} in the normal cross sections along the P-2 and P-4 paths. The black line indicates the FZ boundary.

melting point. This scaling approach is a simplification, as lowering the laser power would not only reduce the peak temperature but also alter the temperature gradients and distribution, and such effects are not fully captured by a scaling factor. The resulting thermal history along the laser track involves heating and cooling, without the formation of a melt pool and FZ downstream. While simplified, this approach offers a preliminary assessment of how reduced laser power affects stress generation and plastic deformation along the laser track.

CPFE simulations show that reducing the temperature profile to represent lower laser power results in decreased stresses along the laser track. For example, along the P-4 path defined in Fig. 4(a), Fig. 5(a) compares normal and shear stresses (σ_{xx} , σ_{yy} and σ_{xy}) for cases with and without melting. Lower temperatures reduce thermal expansion, thereby decreasing both normal and shear stresses. Additionally, melting resets the plastic history by erasing prior plastic shear strains during solidification, further amplifying the differences in normal stress. Fig. 5(b) shows contour plots of γ_i^{acc} on the six $\{111\}\langle 110 \rangle$ slip systems responsible for generating surface slip traces, demonstrating a significant reduction compared to Fig. 3(a). Based on γ_i^{acc} in Fig. 5(b), the predicted slip traces in Fig. 5(c) match experimental observations in Fig. 5(d) from a 50 W laser scan while keeping the other scan parameters identical to those in Fig. 1(a). These slip traces are similar to those in Fig. 3(c) but cover smaller areas with lower densities. Fig. 5(e) and (f) show reductions in equivalent plastic strains and surface displacements compared to Fig. 4(a) and (b), respectively. Overall, these results suggest that higher laser power generates greater stresses and plastic strains along the laser track.

4.3. $[\bar{1}01]$ and $[10\bar{1}]$ scan directions

For the $[\bar{1}01]$ scan direction, the absence of symmetric slip planes about the track centerline results in asymmetric slip trace distributions, as shown in Fig. 1(b). Our experiments also reveal that slip traces inclined to the laser track exhibit different orientations when scanning along $[\bar{1}01]$ and its reverse direction, $[10\bar{1}]$. To capture these effects, we performed CPFE simulations for both scan directions. Since thermal conductivity is typically isotropic in cubic crystals, we used the same moving temperature profile as for the $[\bar{1}2\bar{1}]$ scan direction and adopted the same coordinate system definition used previously, namely, $x\text{-}[\bar{1}\bar{2}\bar{1}]$, $y\text{-}[\bar{1}01]$, and $z\text{-}[111]$.

For the $[\bar{1}01]$ scan direction, Fig. 6(a1-a3) show contour plots of in-plane normal and shear stresses. Due to the absence of slip-plane symmetry, σ_{xx} and σ_{yy} lose symmetry about the track centerline, while σ_{xy} deviates from anti-symmetry. Despite these deviations, the stress distributions resemble those for the $[\bar{1}2\bar{1}]$ scan direction, reflecting similar driving forces: heating-induced expansion ahead of the melt pool and cooling-induced contraction downstream along the laser track. Fig. 6(b) shows contour plots of γ_i^{acc} on the six $\{111\}\langle 110 \rangle$ slip systems responsible for generating surface slip traces, numbered as in Fig. 1(d). Unlike the stress fields, these γ_i^{acc} contours differ significantly from those in Fig. 3(a). This is primarily because the two scan directions differ by a 90° rotation about the $[111]$ surface normal, which alters the relative orientations of the six slip systems with respect to the scan path.

For the reverse $[10\bar{1}]$ scan direction, Fig. 6(c1-c2) show contour plots of in-plane normal stresses, which are mirror reflections (about the x -axis) of those in Fig. 6(a1-a2). By contrast, the shear stress contours in

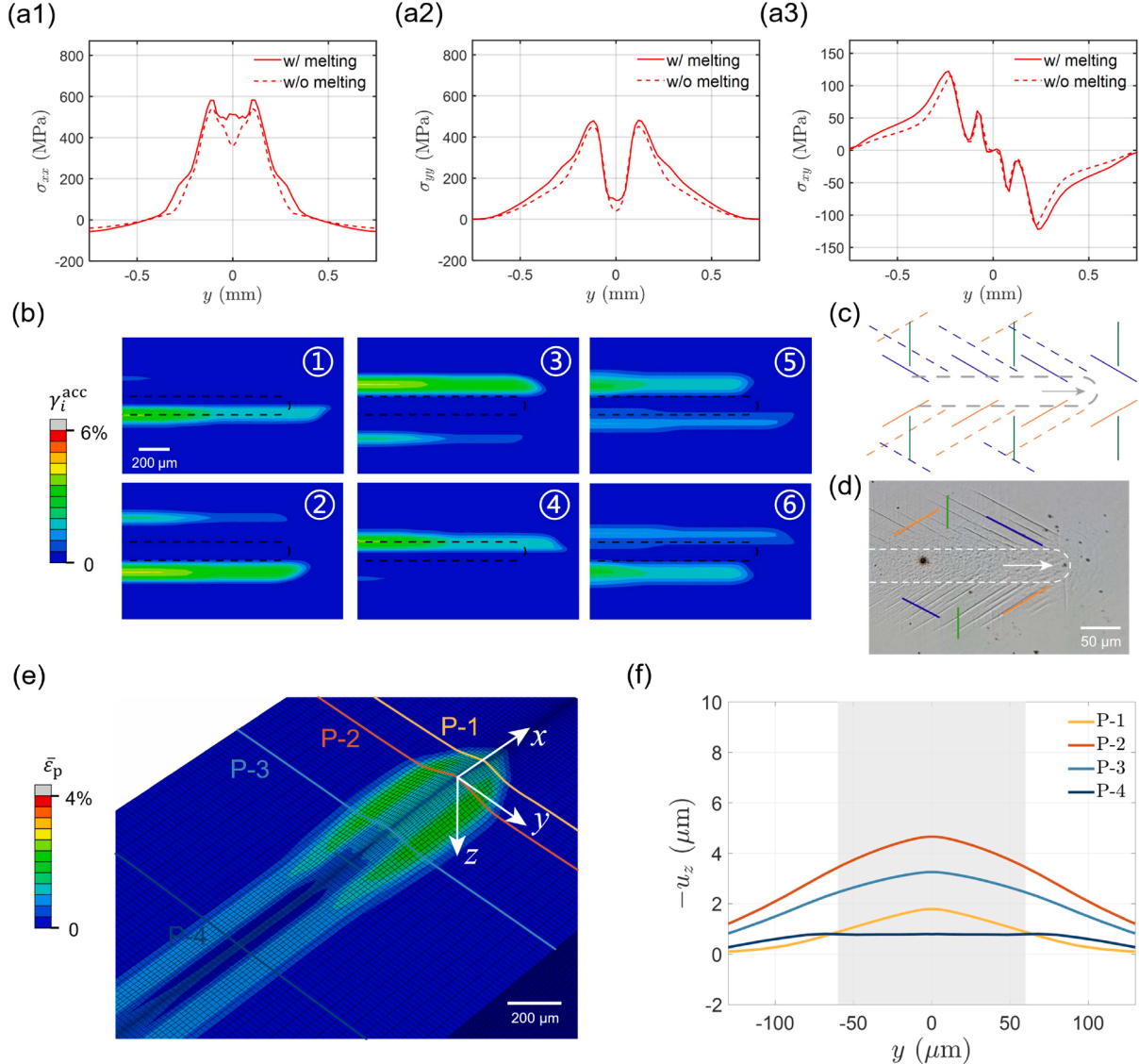


Fig. 5. CPFE results by a reduced temperature profile for laser scanning along the x-[12̄1] direction. (a) Comparison of (a1) σ_{xx} , (a2) σ_{yy} , and (a3) σ_{xy} distribution along P-4 in Fig. 4(a) with and without melting. (b) Contour plots of γ_i^{acc} on the top surface on the six $\{111\}\langle110\rangle$ slip systems responsible for generating surface slip traces. (c) Predicted distributions of slip traces along the laser track. (d) Experimental observations of slip traces from a 50 W laser scan track without melting. (e) Contour plot of equivalent plastic strain ($\bar{\varepsilon}_p$) on the deformed surface, with nodal displacements amplified 10 times for clear visualization. (f) surface displacement ($-u_z$) against the z-coordinate along the P-1 to P-4 paths in (e) crossing the laser track (same path locations as those in Fig. 4(a)).

Fig. 6(a3) and (c3) display anti-symmetry with respect to the x-axis, as schematically illustrated in Fig. 6(e). The corresponding γ_i^{acc} contour plots are shown in Fig. 6(d).

From the location and magnitude of γ_i^{acc} for each scan direction, we predicted the distributions of slip traces along the [101] track (Fig. 6(f)) and the [10̄1] track (Fig. 6(h)), both of which are consistent with the experimental observations in Fig. 6(g) and 6(i), respectively. Notably, the slip-trace pattern in Fig. 6(g) (illustrated in Fig. 6(f)) is related to that in Fig. 6(i) (illustrated in Fig. 6(h)) through a mirror reflection about the x-axis, rather than a 180° rotation about the [111] surface normal, owing to the anti-symmetry of the shear stresses shown in Fig. 6(a3) and (c3).

5. Concluding remarks

The study of plastic deformation of laser-processed crystalline materials is critical for understanding the effects of plastic anisotropy, irreversibility, and their temperature dependence on thermomechanical

behavior during AM processing. These factors significantly affect stress evolution, distortion, defect formation, and material degradation in AM parts. In this study, we use optical microscopy to visualize plastic deformation along laser tracks in Ni single crystals. Slip traces generated on the (111) surface under laser scans along the [12̄1], [101] and [10̄1] directions are examined. Their distributions reveal the extent and nature of plastic shear caused by dislocation activity on different slip systems during heating and cooling associated with laser scanning.

To simulate laser scanning processes, we apply a temperature-dependent CPFE model that accounts for thermal softening, melting, solidification, thermally induced expansion and contraction, and plastic shear on $\{111\}\langle110\rangle$ slip systems in FCC Ni. The CPFE results align closely with the experimentally observed slip trace patterns. Additionally, the distributions of accumulated plastic shear strain are used to identify the slip planes and slip directions responsible for generating distinct slip trace morphologies. The CPFE results connect surface slip traces to subsurface plastic deformation and predict transient and residual surface distortion, linking them to subsurface stress evolution.

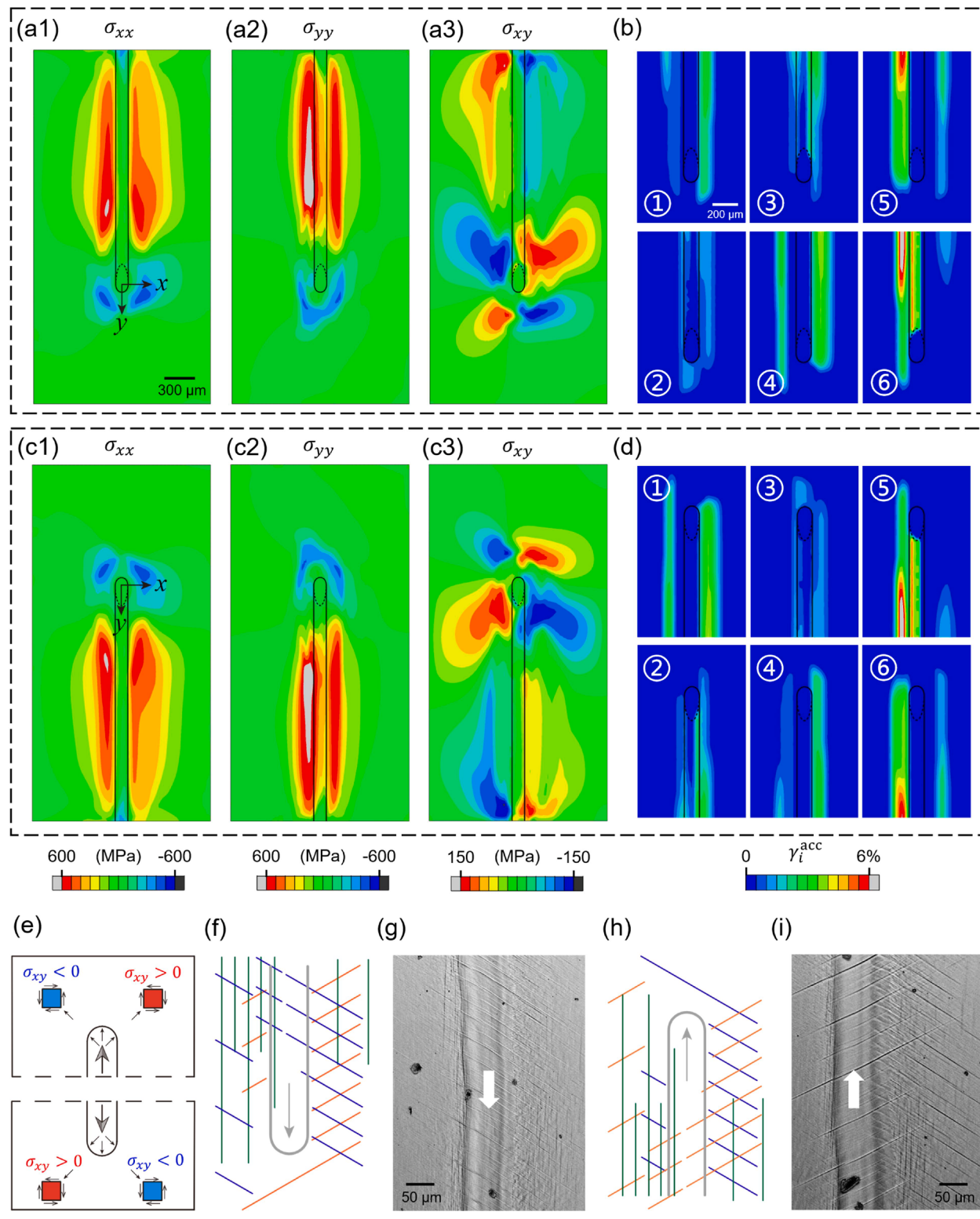


Fig. 6. CPFE results for stresses, accumulated shear strains (γ_i^{acc}), and slip traces on the top surface for laser scanning along the $\bar{1}01$ and $10\bar{1}$ scan directions. Contour plots of (a1-a3) σ_{xx} , σ_{yy} , σ_{xy} , and (b) γ_i^{acc} on each of six $\{111\}\langle 110 \rangle$ slip systems responsible for generating surface slip traces for the $\bar{1}01$ scan. Contour plots of (c1-c3) σ_{xx} , σ_{yy} , σ_{xy} , and (d) γ_i^{acc} on each of the six $\{111\}\langle 110 \rangle$ slip systems responsible for generating surface slip traces for the $10\bar{1}$ scan. (e) Schematic illustration of the shear stress state ahead of the laser beam for the $\bar{1}01$ and $10\bar{1}$ scan directions. (f) CPFE predictions and (g) Experimental observations of slip traces for the $\bar{1}01$ scan. and (h) CPFE predictions and (i) Experimental observations of slip traces for the $10\bar{1}$ scan.

These results validate the CPFE model and provide insights into controlling thermomechanical responses in laser-based AM processes.

The present study can be extended to single crystals and polycrystals with different lattice structures and alloy compositions under diverse scanning conditions, addressing the coupling between slip trace patterns and the complex evolution of grains, sub-grain structures, and dendrites during laser scanning [21,22]. Future modeling efforts should integrate transient heat transfer analysis with CPFE simulations to fully capture the thermomechanical response. Model predictions can be validated using *in situ* experiments such as synchrotron X-ray diffraction and high-resolution digital image correlation [32]. Given the critical role of crystalline anisotropy and slip activity, CPFE simulations can also provide a means to assess the applicability of simplified reduced order models (e.g., isotropic plasticity) that may be used to promote more efficient large-scale simulations of laser-processing. Coupled experimental and computational studies will ultimately advance predictive modeling and optimization of laser-based AM, leading to improved material properties and part performance.

CRediT authorship contribution statement

Yazhuo Liu: Writing – original draft, Visualization, Validation, Methodology, Investigation, Formal analysis, Data curation. **Kunqing Ding:** Methodology, Investigation, Formal analysis. **Andrew J. Birnbaum:** Visualization, Validation, Methodology, Investigation, Formal analysis, Data curation. **Anna Rawlings:** Visualization, Validation, Methodology, Investigation, Formal analysis, Data curation. **Audrey Sun:** Investigation, Data curation. **Wen Chen:** Investigation, Formal analysis. **David L. McDowell:** Writing – review & editing, Supervision, Project administration, Investigation, Funding acquisition, Formal analysis, Conceptualization. **John G. Michopoulos:** Supervision, Investigation, Funding acquisition, Formal analysis. **Ting Zhu:** Writing – review & editing, Writing – original draft, Supervision, Project administration, Investigation, Funding acquisition, Conceptualization.

Declaration of competing interest

The authors declare that they have no known competing financial interests or personal relationships that could have appeared to influence the work reported in this paper.

Acknowledgments

YL, KD, TZ and DLM acknowledge support by the Office of Naval Research under the Agile ICME Toolkit project (N00014–18–1–2784). AJB, AR and JGM acknowledge support by the Office of Naval Research through the Naval Research Laboratory’s core funding, and the Office of Naval Research under the Agile ICME Toolkit project (N0001420WX00405). WC acknowledges support by the National Science Foundation (DMR-2516195 and DMR-2516550).

References

- [1] T. DebRoy, H.L. Wei, J.S. Zuback, T. Mukherjee, J.W. Elmer, J.O. Milewski, A. M. Beese, A. Wilson-Heid, A. De, W. Zhang, Additive manufacturing of metallic components – Process, structure and properties, *Prog. Mater. Sci.* 92 (2018) 112–224.
- [2] W.E. Frazier, Metal additive manufacturing: a review, *J. Mater. Eng. Perform.* 23 (6) (2014) 1917–1928.
- [3] Y.M. Wang, T. Voisin, J.T. McKeown, J. Ye, N.P. Calta, Z. Li, Z. Zeng, Y. Zhang, W. Chen, T.T. Roehling, R.T. Ott, M.K. Santala, P.J. Depond, M.J. Matthews, A. V. Hamza, T. Zhu, Additively manufactured hierarchical stainless steels with high strength and ductility, *Nat. Mater.* 17 (2018) 63–71.
- [4] T.D. Ngo, A. Kashani, G. Imbalzano, K.T.Q. Nguyen, D. Hui, Additive manufacturing (3D printing): a review of materials, methods, applications and challenges, *Compos. B Eng* 143 (2018) 172–196.
- [5] S. Cooke, K. Ahmadi, S. Willerth, R. Herring, Metal additive manufacturing: technology, metallurgy and modelling, *J. Manuf. Process.* 57 (2020) 978–1003.
- [6] R. Cunningham, C. Zhao, N. Parab, C. Kantzios, J. Pauza, K. Fezzaa, T. Sun, A. D. Rollett, Keyhole threshold and morphology in laser melting revealed by ultrahigh-speed x-ray imaging, *Science* 363 (2019) 849–852.
- [7] H.L. Wei, T. Mukherjee, W. Zhang, J.S. Zuback, G.L. Knapp, A. De, T. DebRoy, Mechanistic models for additive manufacturing of metallic components, *Prog. Mater. Sci.* 116 (2021) 100703.
- [8] A. Mostafaei, C. Zhao, Y. He, S. Reza Ghiasi, B. Shi, S. Shao, N. Shamsaei, Z. Wu, N. Kouraytem, T. Sun, J. Pauza, J.V. Gordon, B. Webler, N.D. Parab, M. Asherloo, Q. Guo, L. Chen, A.D. Rollett, Defects and anomalies in powder bed fusion metal additive manufacturing, *Curr. Opin. Solid State Mater. Sci.* 26 (2022) 100974.
- [9] C. Zhao, B. Shi, S. Chen, D. Du, T. Sun, B.J. Simonds, K. Fezzaa, A.D. Rollett, Laser melting modes in metal powder bed fusion additive manufacturing, *Rev. Mod. Phys.* 94 (2022) 045002.
- [10] L. Gao, Y. Chen, X. Zhang, S.R. Agnew, A.C. Chuang, T. Sun, Evolution of dislocations during the rapid solidification in additive manufacturing, *Nat. Commun.* 16 (2025) 4696.
- [11] F. Schmeiser, E. Krohmer, N. Schell, E. Uhlmann, W. Reimers, Experimental observation of stress formation during selective laser melting using *in situ* X-ray diffraction, *Addit. Manuf.* 32 (2020) 101028.
- [12] W. Chen, T. Voisin, Y. Zhang, J.-B. Florien, C.M. Spadaccini, D.L. McDowell, T. Zhu, Y.M. Wang, Microscale residual stresses in additively manufactured stainless steel, *Nat. Commun.* 10 (2019) 4338.
- [13] Z. Wang, E. Denlinger, P. Michaleris, A.D. Stoica, D. Ma, A.M. Beese, Residual stress mapping in Inconel 625 fabricated through additive manufacturing: method for neutron diffraction measurements to validate thermomechanical model predictions, *Mater. Des.* 113 (2017) 169–177.
- [14] J.L. Bartlett, B.P. Croom, J. Burdick, D. Henkel, X. Li, Revealing mechanisms of residual stress development in additive manufacturing via digital image correlation, *Addit. Manuf.* 22 (2018) 1–12.
- [15] T.J. Ruggles, Y.S.J. Yoo, B.E. Dunlap, M.A. Crimp, J. Kacher, Correlating results from high resolution EBSD with TEM- and ECPI-based dislocation microscopy: approaching single dislocation sensitivity via noise reduction, *Ultramicroscopy* 210 (2020) 112927.
- [16] G. Vastola, G. Zhang, Q.X. Pei, Y.W. Zhang, Controlling of residual stress in additive manufacturing of Ti6Al4V by finite element modeling, *Addit. Manuf.* 12 (2016) 231–239.
- [17] T. Mukherjee, W. Zhang, T. DebRoy, An improved prediction of residual stresses and distortion in additive manufacturing, *Comput. Mater. Sci.* 126 (2017) 360–372.
- [18] Y. Zhang, K. Ding, Y. Gu, W. Chen, Y.M. Wang, J. El-Awady, D.L. McDowell, T. Zhu, Modeling of microscale internal stresses in additively manufactured stainless steel, *Model. Simul. Mater. Sci. Eng.* 30 (2022) 074001.
- [19] N. Mohanan, J.G.S. Macias, J. Bleyer, T. Helfer, M.V. Upadhyay, Intergranular stress and plastic strain formation during laser scanning of additively manufactured stainless steel: an experimentally-driven thermomechanical simulation study, *Materialia* 34 (2024) 102082.
- [20] A.J. Birnbaum, A.K. Rawlings, J.C. Steuben, A. Iliopoulos, J.G. Michopoulos, Plastic strain visualization and analysis of Laser-Processed nickel single crystals, *Mater. Lett.* 349 (2023) 134752.
- [21] M. Rappaz, S.A. David, J.M. Vitek, L.A. Boatner, Development of microstructures in Fe–15Ni–15Cr single crystal electron beam welds, *Metall. Trans. A* 20 (1989) 1125–1138.
- [22] H.L. Wei, J.W. Elmer, T. DebRoy, Crystal growth during keyhole mode laser welding, *Acta Mater.* 133 (2017) 10–20.
- [23] M. Rabaud, F. Moisy, Ship wakes: kelvin or Mach angle? *Phys. Rev. Lett.* 110 (2013) 214503.
- [24] S.R. Kalidindi, C.A. Bronkhorst, L. Anand, Crystallographic texture evolution in bulk deformation processing of fcc metals, *J. Mech. Phys. Solids* 40 (1992) 537–569.
- [25] F.T. Meissonnier, E.P. Busso, N.P. O’Dowd, Finite element implementation of a generalised non-local rate-dependent crystallographic formulation for finite strains, *Int. J. Plast.* 17 (2001) 601–640.
- [26] M. Kothari, L. Anand, Elasto-viscoplastic constitutive equations for polycrystalline metals: applications to tantalum, *J. Mech. Phys. Solids* 46 (1998) 51–83.
- [27] U.F. Kocks, A.S. Argon, M.F. Ashby, Thermodynamics and kinetics of slip, *Prog. Mater. Sci.* 19 (1975) 1–281.
- [28] J.C. Ion, H.R. Shercliff, M.F. Ashby, Diagrams for laser materials processing, *Acta Metall. Mater.* 40 (1992) 1539–1551.
- [29] R.B. Patil, V. Yadava, Finite element analysis of temperature distribution in single metallic powder layer during metal laser sintering, *Int. J. Mach. Tools. Manuf.* 47 (7) (2007) 1069–1080.
- [30] P. Zagade, B.P. Gautham, A. De, T. DebRoy, Analytical estimation of fusion zone dimensions and cooling rates in part scale laser powder bed fusion, *Addit. Manuf.* 46 (2021) 102222.
- [31] Y.Z. Xia, H. Bei, Y.F. Gao, D. Catoor, E.P. George, Synthesis, characterization, and nanoindentation response of single crystal Fe–Cr–Ni alloys with FCC and BCC structures, *Mater. Sci. Eng. A* 611 (2014) 177–187.
- [32] J.C. Stinville, M.A. Charpagne, R. Maaß, H. Proudhon, W. Ludwig, P.G. Callahan, F. Wang, I.J. Beyerlein, M.P. Echlin, T.M. Pollock, Insights into plastic localization by crystallographic slip from emerging experimental and numerical approaches, *Annu. Rev. Mater. Res.* 53 (2023) 275–317.